The Astrophysical Journal, 937:126 (14pp), 2022 October 1 https://doi.org/10.3847/1538-4357/ac86d7

Stellar Energetic Particle Transport in the Turbulent and CME-disrupted Stellar Wind of AU Microscopii

Federico Fraschetti[1,2], Julián D. Alvarado-Gómez[3], Jeremy J. Drake[1], Ofer Cohen[4], and Cecilia Garraffo[1]
[1] Center for Astrophysics | Harvard & Smithsonian, 60 Garden Street, Cambridge, MA, 02138, USA; federico.fraschetti@cfa.harvard.edu
[2] Dept. of Planetary Sciences-Lunar and Planetary Laboratory, University of Arizona, Tucson, AZ, 85721, USA
[3] Leibniz Institute for Astrophysics Potsdam, An der Sternwarte 16, D-14482 Potsdam, Germany
[4] University of Massachusetts at Lowell, Department of Physics & Applied Physics, 600 Suffolk Street, Lowell, MA, 01854, USA
Received 2022 June 6; revised 2022 July 27; accepted 2022 July 28; published 2022 October 5

Abstract

Energetic particles emitted by active stars are likely to propagate in astrospheric magnetized plasma and disrupted by the prior passage of energetic coronal mass ejections (CMEs). We carried out test-particle simulations of ∼GeV protons produced at a variety of distances from the M1Ve star AU Microscopii by coronal flares or traveling shocks. Particles are propagated within a large-scale quiescent three-dimensional magnetic field and stellar wind reconstructed from measured magnetograms, and within the same stellar environment following the passage of a 10^{36} erg kinetic energy CME. In both cases, magnetic fluctuations with an isotropic power spectrum are overlayed onto the large-scale stellar magnetic field and particle propagation out to the two innnermost confirmed planets is examined. In the quiescent case, the magnetic field concentrates the particles into two regions near the ecliptic plane. After the passage of the CME, the closed field lines remain inflated and the reshuffled magnetic field remains highly compressed, shrinking the scattering mean free path of the particles. In the direction of propagation of the CME lobes the subsequent energetic particle (EP) flux is suppressed. Even for a CME front propagating out of the ecliptic plane, the EP flux along the planetary orbits highly fluctuates and peaks at ∼2–3 orders of magnitude higher than the average solar value at Earth, both in the quiescent and the post-CME cases.

Unified Astronomy Thesaurus concepts: Exoplanets (498)

1. Introduction

Active low-mass K- and M-star circumstellar environments are affected, with an occurrence rate much higher than Solar, by violent eruptions producing either very energetic coronal flares (Youngblood et al. 2017; Jackman et al. 2020) or possibly escaping coronal mass ejections (CMEs; $> 10^{31}$ erg kinetic energy) detected, e.g., via X-ray spectroscopy (Argiroffi et al. 2019). CME candidates are also traced via Doppler shifts in Balmer lines (Houdebine et al. 1990) or asymmetries therein (Vida et al. 2019), continuous X-ray absorption during the flare (Moschou et al. 2019), or dimming in the extreme ultraviolet (EUV) and X-ray ranges due to CME mass loss (Veronig et al. 2021). The broadband flare emission (from radio to γ-rays), hence the bolometric detectable energy output, from such stars is routinely investigated (e.g., Paudel et al. 2021) whereas the kinetic energy of the associated CMEs has been estimated only in a handful of cases (e.g., Moschou et al. 2019). Within the heliosphere, charged particle acceleration at CME-driven shocks has been accurately determined via in situ measurements to drain ∼10% of the total CME energy, regardless of the magnetic obliquity at the shock (David et al. 2022). Comparable energy fractions might be expected for active stars.

The passage of a CME compresses and breaks magnetic field lines leading to a rearrangement of the large-scale magnetic field topology throughout the astrosphere, from the corona to the interplanetary region, that is traversed by charged particles energized close to the star. Such a disrupted configuration of the stellar wind is more likely to be encountered by outwardly propagating energetic particles (hereafter EPs) from active stars due to a flaring rate much higher than solar (Youngblood et al. 2017). The flux of EPs into habitable zone (hereafter HZ) planets in the quiescent winds of active stars was first determined numerically for the case of TRAPPIST-1 (Fraschetti et al. 2019). The flux exceeded the solar value by ∼4 orders of magnitude. However, the passage of a very energetic CME is expected to reshuffle the wind magnetic field over large angular regions out to large distances. To our knowledge, the effect of such a phenomenon has not yet been investigated.

The James Webb Space Telescope (JWST) is expected to open up new pathways toward the observational studies of exoplanet habitability and atmosphere composition and evolution. In particular, exoplanets with radii between 1.7 and 3.5 times the Earth's radius (i.e., sub-Neptunes) are favorable targets for HZ planet search instead of smaller planets as the larger amount of atmospheric H_2 acts as a greenhouse gas allowing for stable liquid water (Pierrehumbert & Gaidos 2011; Hu et al. 2021). Morevoer, sub-Neptunes could populate the so-called "evaporation valley", possibly resulting from atmospheric photoevaporation due to high-energy radiation (EUV, X-ray) from the host star (Owen & Wu 2013).

We focus here on AU Microscopii (AU Mic), an M dwarf with flaring activity observed by, e.g., the Hubble Space Telescope (HST) in the far-ultraviolet (far-UV) (Redfield et al. 2002) or XMM Newton in X-rays (Magee et al. 2003) and a modeled connection between flares (Extreme Ultraviolet Explorer; Cully et al. 1994) and ejected plasmoids self-similarly expanding in a CME fashion. The confirmation of two sub-Neptunian planets orbiting AU Mic (Martioli et al. 2021) makes the system particularly attractive for investigating the effects of CME passage on EP propagation from star to planet

due to their impact on planetary atmospheres and their evaporation (Fulton et al. 2017).

The diffusive transport of EPs originating from solar eruptions is known to be governed by the unperturbed large-scale magnetic field and by its small-scale fluctuations (Jokipii 1966). Existing numerical analyses of the propagation of EPs from young stars surrounded by proto-planetary disks (Rab et al. 2017; Rodgers-Lee et al. 2017; Fraschetti et al. 2018; Gaches & Offner 2018; Padovani et al. 2018) or in exoplanetary environments (Fraschetti et al. 2019) have focused on quiescent stellar conditions. Particle transport is determined by integrating EP trajectories in synthetic three-dimensional (3D) turbulence (Fraschetti et al. 2019) or by solving a suitable transport equation, as done recently by Hu et al. (2022). However, as mentioned above, EP propagation into a realistic astrosphere disrupted by a recent (within 1–2 hr) CME passage does not appear to have been discussed previously.

In this paper, we perform a detailed analysis of the propagation of charged particles energized in the proximity of AU Mic, i.e., by flares or CME-shocks, through a magnetized stellar wind calculated via the Space Weather Modeling Framework (SWMF) codes, in particular the Alfvén Wave Solar Model (AWSoM; van der Holst et al. 2014), out to the second confirmed planet. A synthetic turbulent magnetic field is added to the large-scale unperturbed component (Fraschetti et al. 2019). The propagation within the quiescent state astrosphere is compared with the propagation 90 minutes after the passage of a very energetic CME; a kinetic energy consistent with the best candidate event observed in this star so far ($\sim 10^{36}$ erg) is adopted (Katsova et al. 1999; Alvarado-Gómez et al. 2022).

The EP flux along the planetary orbits is found to fluctuate highly and peak at ∼2–3 orders of magnitude higher than the average solar value at Earth, both in the quiescent and the post-CME cases. This excess has to be compared with the ∼4 orders of magnitude in EP flux excess at the closer-in HZ planets of the more active TRAPPIST-1, as first determined by Fraschetti et al. (2019).

The outline of this paper follows: in Section 2 the observational properties of the AM Mic planetary system are summarized; in Section 3 the assumptions on the stellar EP origin and propagation properties are emphasized along with the generated magnetic turbulence with intensity and injection scale as parameters. In Section 4 the main results are presented for the cases of winds in quiescent state (with particles injected as close as the lower corona) and post-CME state. In Section 5 the EP fluxes impinging on the planets AU Mic b and c for the quiescent and post-CME case are compared, and the EPs transport properties for AU Mic and TRAPPIST-1 are also compared. Section 6 draws the conclusions of this work.

2. The Large-scale Magnetized Wind of AU Mic

AU Microscopii is a bright, nearby (magnitude[5] = 8.6, d = 9.72 ± 0.04 pc; Gaia Collaboration et al. 2018) M dwarf with mass of $M_\star = 0.5\,M_\odot$, a radius of $R_\star = 0.75\,R_\odot = 5.18 \times 10^{10}$ cm (Plavchan et al. 2020), and a rotation period of 4.85 days (Torres et al. 1972). A spatially resolved edge-on debris disk surrounds the star with a ∼50 au inner radius (Kalas et al. 2004). Transiting Exoplanet Survey Satellite (TESS) light curves confirmed that AU Mic hosts a Neptune-size planet (AU Mic b; Plavchan et al. 2020) with a radius of $1.05\,R_N = 2.6 \times 10^9$ cm (where R_N is Neptune's radius), a mass of $1.00\,M_N$ (with M_N is the Neptune mass), an orbital distance of $R_b = 0.065$ au $= 19.1\,R_\star = 9.89 \times 10^{11}$ cm (orbits are assumed to be circular; Martioli et al. 2021), an orbital period of 8.46 days (Martioli et al. 2021; Klein et al. 2021b), an inclination angle of the magnetic field/stellar rotation axis of ∼19° (Klein et al. 2021b), and an uncertain alignment between the spin axis of the host star and the orbital vector axis of the planet (Addison et al. 2021). TESS revealed also a second orbiting Neptune-size planet (AU Mic c) with a radius of $0.84\,R_N = 2.07 \times 10^9$ cm, a mass of $0.13\,M_N < M_c < 1.46\,M_N$, an orbital distance of $R_c = 0.11$ au $= 29\,R_\star = 1.5 \times 10^{12}$ cm, and an orbital period of 18.8 days (Martioli et al. 2021). The planetary orbital plane for both planets is located within 1° from the stellar equator (Martioli et al. 2021).

The 3D magnetized quiescent stellar wind (hereafter SW) was computed using the SWMF codes (Tóth et al. 2005; van der Holst et al. 2014; Gombosi et al. 2018), evolved from the BATS-R-US MHD code (Powell et al. 1999) that was originally developed for the solar corona. The code uses as an inner boundary condition a magnetogram (for details see Alvarado-Gómez et al. 2022) describing the surface distribution of the radial magnetic field in the quiescent state and calculates the coronal heating and SW acceleration due to Alfvén wave turbulence dissipation, taking into account radiative cooling and electron heat conduction. The model has been validated with solar wind observations (Cohen et al. 2008); improvements of wave dissipation to electron and anisotropic proton heating led to good agreement with the magnetic field measured by the Parker Solar Probe (PSP) (van der Holst et al. 2022). Further validations have been based on remote observations in solar minimum (Sachdeva et al. 2019) and maximum (Sachdeva et al. 2021) conditions. The code has been adapted and used to simulate SWs and the space weather environments of exoplanets (e.g., Vidotto et al. 2015; Garraffo et al. 2017; Cohen et al. 2020; Evensberget et al. 2021), and has also been used to simulate CME eruptions from highly magnetized stars (e.g., Cohen et al. 2011; Alvarado-Gómez et al. 2018, 2019, 2020, 2022) and the associated radio emission in ϵ Eridani (Fionnagáin et al. 2022).

Stellar surface magnetic field distributions needed to drive stellar wind simulations have generally been based on Zeeman–Doppler Imaging (ZDI) observations. The large-scale magnetic field (B-field) of AU Mic derived in such a way suffers from some uncertainties. Kochukhov & Reiners (2020) have shown that the use of distinct polarizations (circular and linear) from the ESPaDOnS and HARPSpol instruments in ZDI maps leads to magnetic field strengths differing by a factor 10 (184 G and 2 kG, respectively). Using SPIRou polarization observations, Klein et al. (2021b) found a 450 G large-scale dipole field inclined by ∼20° with respect to the rotation axis. Both maps were used in a companion paper (Alvarado-Gómez et al. 2022) as an inner boundary to generate the 3D magnetized SW of AU Mic, both in quiescent and CME-disrupted phases; in the present work, we have used the B-field produced in the cases 1 and 3 therein. Cohen et al. (2022), using the same wind reconstruction, have determined the variations in Lyα absorption signatures during transits of AU Mic b due to the passage of a very energetic CME. The Klein et al. (2021b) maps are also implemented by Kavanagh et al. (2021) to generate, via

[5] http://simbad.u-strasbg.fr/simbad/sim-id?Ident=Au+Mic

AWSOM, the AU Mic 2 two distinct winds with two distinct ratios of the Alfvén flux-to-magnetic strength (that produce two distinct values of mass loss) to constrain the radio emission. In Alvarado-Gómez et al. (2022) one value of the Alfvén flux-to-magnetic strength ratio was used. Since the 3D structures of the two Alfvén surfaces determined by Kavanagh et al. (2021) are different in shape and extension to each other and, arguably, different from the Alfvén surface determined by Alvarado-Gómez et al. (2022), EP transport is expected to be different in these three cases due to the structure of the region of transition between closed and open field lines.

In this paper, we calculate the propagation of stellar EPs within the turbulent magnetized SW of AU Mic driven via the ZDI maps from Klein et al. (2021b) and Kochukhov & Reiners (2020). In addition to the quiescent SW, we have produced a number of SW configurations disrupted by very energetic CMEs (kinetic energy $\sim 10^{36}$ erg; Alvarado-Gómez et al. 2022) propagating throughout the entire simulation box. The CME structure is initialized by using the Titov & Démoulin (1999) flux-rope eruption model over the AWSoM field background. We consider herein one such configuration in detail: stellar EPs are propagated within SW snapshots 90 minutes after the CME initialization, i.e., when the CME front has reached regions $>100\,R_\star$. EPs travel much faster than the CME front and the choice of 90 minutes ensures that the astrosphere has been disrupted by the CME as far as the numerical calculation allows.

3. Stellar Energetic Particles In the Turbulent Environment of AU Mic

3.1. Assumptions For EPs: Origin, Propagation, and Abundance

The goal of this work is to compare the transport of EPs in a quiescent SW environment of a young active star with the transport within the same environment 90 minutes after the passage of an extraordinarily energetic CME (compared with heliospheric scales).

In the solar context, GOES measurements of proton enhancements at 1 au confirm that EPs might originate both from solar X-ray (SXR) flares and CME-driven shocks (Belov et al. 2007). Guided by these heliospheric observations, we assume that young active stars produce EPs via two distinct processes: (1) CME-driven shocks, traveling through the interplanetary medium and therein accelerating EPs, a certain fraction of which are likely to escape the shock at various distances from the host star; and (2) coronal flares that release EPs locally accelerated close to the stellar surface. Presumably via different mechanisms, namely diffusive shock acceleration for the former and magnetic reconnection for the latter, both processes contribute multi-MeV to $\sim$GeV kinetic energy protons in the heliosphere.

We inject EPs on spherical surfaces with radii of $R_s = 2\,R_\star$ and $5\,R_\star$ concentric with the star, to compare the effect of the injection at two locations where the relative amount of closed-to-open field lines changes with a large spatial gradient; the diffusion in that region determines the EP flux at the planets. Following the approach of Fraschetti et al. (2019), we calculate the time-forward propagation of test particles by using two distinct magnetostatic SW configurations: (1) a quiescent interplanetary magnetic field and the (2) stellar magnetic field 90 minutes after the initiation of a very energetic CME; in both cases we include the same overlapping small-scale turbulence (see Section 4.4).

The modeling of the TESS flaring rate for AU Mic (Gilbert et al. 2022) is consistent with one flare every 3.8 hr for a flux between 0.06% and 1.5% of the stellar flux (Martioli et al. 2021). For AU Mic's bolometric luminosity of $0.09\,L_\odot$ (Plavchan et al. 2009), these correspond to fluxes at AU Mic b of 1.8×10^4 erg cm^{-2} s^{-1} sr^{-1} and 4.4×10^5 erg cm^{-2} s^{-1} sr^{-1}, respectively, and, possibly, to very energetic associated CMEs. Thus, the 90 minutes interval elapsed since the CME initialization allows the CME front to reach $R > 100\,R_\star$ before the eruption of a subsequent energetic CME, consistently with observations (Gilbert et al. 2022). On the other hand, due to the high flaring occurrence in active stars, i.e., a likely high rate of associated CMEs, a wind configuration disrupted by a CME has a higher filling factor than for the Sun; therefore a significant fraction of EPs originating from the host star encounters typically a non-quiescent wind. In contrast, due to the lower level of solar activity, in the heliosphere most of the EP transport occurs within a quiescent, rather than a CME-disrupted, wind.

The magnetostatic approximation adopted herein is justified as follows. The MHD wind solution and the magnetic turbulence are stationary on the timescale of EP propagation to a good approximation. The EPs travel close to the speed of light whereas the stellar rotation period of 4.86 days and radius of $0.75\,R_\odot$ (Klein et al. 2021b) imply a surface stellar rotation speed of a few kilometers per second; the Alfvén speed in the circumstellar medium is at most a few thousand kilometers per second throughout the simulation box, which is much smaller than the EPs' speed.

The EP abundance in the circumstellar medium at a given distance from the host star cannot be constrained through direct observation; instead, we use the estimate based on solar scaling relations between the EP fluence and far-UV and SXR fluence during flares by Youngblood et al. (2017); see Section 5 below. This scaling provides a time-averaged EP enrichment for timescales comparable with a statistically typical flare duration (Vida et al. 2017). A scaling relation of the starspot size with the effective stellar temperature allowed to constrain the abundance of EPs (Herbst et al. 2021). We have verified that a total number of EPs of $N_{\rm inj} = 10{,}240$ yields numerical convergence in all cases presented herein.

Finally, we note that the AU Mic detected debris disk is not expected to impact the EP transport as the inner radius of the disk is measured to be 50 au (Kalas et al. 2004), which is much greater than R_c.

3.2. Turbulent Stellar Magnetic Field

Leveraging the universality of the Kolmogorov scaling within the turbulent inertial range (Armstrong et al. 1995), we assume that the magnetic fluctuations around AU Mic support a 3D Kolmogorov isotropic power spectrum (see also Fraschetti et al. 2019). Spectral analysis of PSP measurements near the minimum of solar cycle 25 in the quiescent inner heliosphere (as close as 0.2 au to the Sun) have shown (Zhao et al. 2020) that the power spectrum of the magnetic turbulence in the direction aligned with the magnetic field is consistent with a Kolmogorov spectral slope of $-5/3$ and is in tension with the -2 slope predicted by the critical balance conjecture (Goldreich & Sridhar 1995); in addition, perpendicular transport in the study of Goldreich & Sridhar (1995) was

found to be inefficient in the perpendicular diffusion of fast particles (Fraschetti 2016a, 2016b). The spectral slope found by PSP confirms previous findings at 1 au from the Wind spacecraft, restricted to fast solar wind (Telloni et al. 2019), and a number earlier analyses (e.g., Jokipii & Coleman 1968).

The total magnetic field is decomposed as $\boldsymbol{B}(x) = \boldsymbol{B}_0(x) + \delta\boldsymbol{B}(x)$, where the large-scale component $\boldsymbol{B}_0(x)$ is the 3D magnetic field generated by the 3D-MHD wind simulations (see Section 2); the random component $\delta\boldsymbol{B} = \delta\boldsymbol{B}(x, y, z)$ has a zero mean ($\langle\delta\boldsymbol{B}(x)\rangle = 0$). As for the turbulent environment of TRAPPIST-1 (Fraschetti et al. 2019), the fluctuation $\delta\boldsymbol{B}(x, y, z)$ is calculated as the sum of plane waves with random orientations, polarizations, and phases following the prescription of Giacalone & Jokipii (1999) and Fraschetti & Giacalone (2012) with an inertial range of $k_{\min} < k < k_{\max}$, with $k_{\max}/k_{\min} = 10^2$, and where $k_{\max}$ is the magnitude of the wavenumber corresponding to the turbulence dissipation scale.

The advantage of the test-particle approach used here is that particle trajectories enable tracking of the pitch-angle scattering, of the perpendicular diffusion, and also of the transport across field lines both in the quiescent and CME-disrupted winds; such effects are known to contribute significantly to particle transport in the heliosphere (e.g., Dröge et al. 2010; Fraschetti & Jokipii 2011; Gómez-Herrero et al. 2015), but are often neglected for analytic tractability. Moreover, a 1D spatial transport equation approach cannot be applied to a wind disrupted by a CME passage as the radial scaling of the diffusion coefficient, κ, typically inferred from the radial scaling of the large-scale magnetic field, is reshuffled in the post-CME wind; the expected strong angular dependence of κ cannot be included in a semi-analytic model.

A second parameter of the stellar wind magnetic turbulence is the correlation length L_c, i.e., the outer scale of turbulence injection. Due to a lack of observational constraints on L_c, and the likely observational inaccessibility to L_c in the near future, in Fraschetti et al. (2019) we used for TRAPPIST-1 a range of values of L_c, each one kept uniform throughout the simulation box, and found no significant difference in the spatial distribution of EPs at the distances corresponding to the semimajor axes of the planets in that system. Likewise, for AU Mic we adopt here the uniform value of $L_c = 10^{-5}$ au throughout the simulation box. Such a value warrants that the resonant scattering condition holds with good approximation during the EP propagation throughout the wind. The resonance condition reads $\mathrm{k} r_g(x)/2\pi = r_g(x)/L_c < 1$ for each wavenumber k within the inertial range; here, $r_g(x) = p_\perp c/eB_0(x)$ is the gyroradius of a proton with $p_\perp$ momentum perpendicular to the unperturbed and space-dependent magnetic field $B_0(x)$, e is the proton electric charge, and c is the speed of light in a vacuum. As for the case of TRAPPIST-1, the combined effect of a high surface stellar magnetic field strength and its decrease with radius make $L_c = 10^{-5}$ au a reasonable value within the assumed circular orbits of AU Mic b and c, for the particle energies considered.

The power, σ^2, of the magnetic fluctuation $\delta B(x)$ relative to $B_0(x)$ is defined as

$$\sigma^2 = (\delta B(x)/B_0(x))^2. \quad (1)$$

Given the current lack of any observational constraint of the magnetic turbulence around AU Mic, it seems reasonable to assume a uniform σ^2, following Fraschetti et al. (2018). Here, σ^2 is assumed to be independent of space throughout the simulation box. The solar wind measurements between 0.3 and 4 au yield for the turbulence amplitude δB a power-law dependence on the heliocentric distance with a comparable slope (-2.2) at a variety of helio-latitudes (Horbury & Tsurutani 2001). In the steady-state reconstructed 3D magnetic fields used here (see Section 2), the spherical average of the unperturbed field $\langle B_0(x)\rangle_\Omega$ drops with radius R as $\sim R^{-2.2}$ (see also the case of TRAPPIST-1 in Fraschetti et al. 2019). The high anisotropy of the post-CME stellar wind due to the CME eruption causes deviations from the monotonic scaling of $\langle B_0(x)\rangle_\Omega$, but it is conceivable that the level of small-scale turbulence is not significantly altered (see Section 4.4 and Kilpua et al. 2021).

The turbulence within the young and active M dwarf magnetosphere is likely to be much stronger than in the solar wind ($\sigma^2 \lesssim 0.1$; Burlaga & Turner 1976), hence the broader σ^2 range of 0.01–1.0 is spanned here. The interpretation of our simulations makes use of the scattering mean free path, $\lambda_\parallel$, given by quasi-linear theory (Jokipii 1966), that reads as (Giacalone & Jokipii 1999; Fraschetti et al. 2018)

$$\lambda_\parallel(x) \simeq 4.8 (r_g(x)/L_c)^{1/3} L_c/\sigma^2. \quad (2)$$

The choices of uniform L_c and σ^2 imply that $\lambda_\parallel$ depends on the spatial coordinates only via $r_g(x)$, i.e., $B_0(x)$. Fitz Axen et al. (2021) investigated the transport of <1 GeV protons within protostellar cores by implementing scattering off magnetic turbulence via a Monte Carlo algorithm that neglects perpendicular transport; thus, cross-field diffusion and consequent longitudinal spread cannot be incorporated. It is noteworthy that assigning L_c and σ^2 for a given particle energy (namely $\lambda_\parallel$) does not uniquely describe the particle transport due to the increase of the perpendicular diffusion as σ^2 increases (Giacalone & Jokipii 1999; Fraschetti & Giacalone 2012; Dröge et al. 2016). Therefore the EPs' trajectories need to be calculated step by step in the given magnetic turbulence without assuming that the EPs follow the magnetic field lines.

4. Results

Here, we discuss the results from injecting 0.1 and 1 GeV kinetic energy protons at $R_s = 2\,R_\star = 0.0069$ au and at $R_s = 5\,R_\star = 0.017$ au for $\sigma^2 = 0.01$ and 1.0. EPs are propagated in our simulations throughout the astrosphere until either they collapse back to the star or hit (for the first time along their trajectory) the spherical surface at $R = R_b$ and $R = R_c$. A small fraction of EPs hit at first the R_b sphere at a latitude different from the geometrical cross section of the planetary orbit, then backscatter and in their subsequent star-ward propagation hit the $R_b(R_c)$ sphere again at the latitude of the planet's orbital plane. Such a fraction is $<1\%$ at most, so is neglected here and the EP trajectories are followed within the region $R < R_c$.

4.1. Quiescent Stellar Wind

In Figure 1 open/closed magnetic field lines are seeded through the orbits of planets b and c. The unperturbed magnetic field lines that approximately track the motions of the EPs have a predominantly dipolar structure (Alvarado-Gómez et al. 2022).

For the quiescent stellar wind numerically reconstructed from the ZDI map from Klein et al. (2021b), Figure 2 shows a

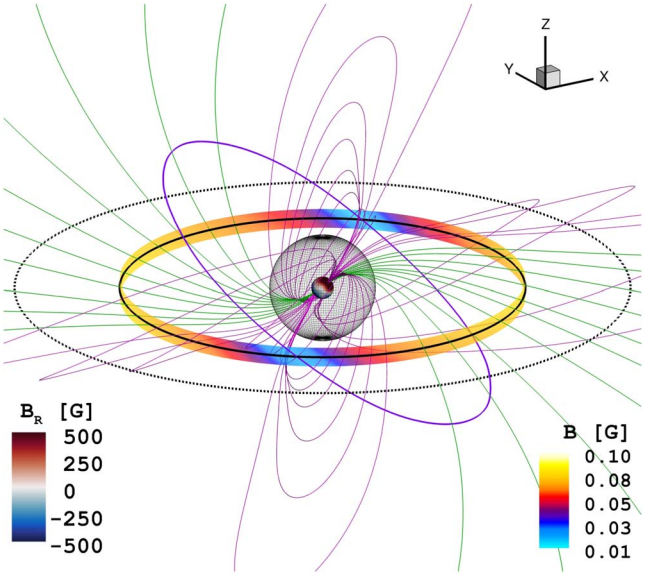

Figure 1. A 3D view of the open (green) and closed (magenta) quiescent stellar wind magnetic field lines. The central sphere is the host star, color coded by the radial component of the local stellar magnetic field on the surface. The transparent gridded sphere marks $R = 5\,R_\star$. The two circles in the equatorial plane mark the orbits of planet b (solid) and c (dotted) around the star. The colored circular ring at $R = R_b$ is color coded with the strength of the large-scale magnetic field. The plane $B_r = 0$ (where B_r is the radial component of the magnetic field), that on average corresponds to the CS, is approximately denoted by the purple tilted circle.

2D histogram in spherical coordinates at two distinct radii ($R = R_b$ and R_c) of the first-crossing points for 1 GeV kinetic energy protons in the case of strong turbulence, i.e., $\sigma^2 = 1$, injected at $R_s = 5\,R_\star$. The corresponding stellar wind magnetic field is shown in Figure 1.

Depleted regions (in blue) reached by no EPs are found at both distances R_b and R_c. Such regions broaden progressively as the distance from the host star increases. The azimuthal oscillation of the depleted regions maps the slow speed wind and the stellar current sheet (CS), both shown in 2D spherical projections of the flow speed and the magnetic field strength in Figure 3; similar correspondence between the EP 2D histogram and the CS was found in the case $\sigma^2 = 1$ for the HZ of the TRAPPIST-1 system (Fraschetti et al. 2019). As for TRAPPIST-1, the depleted regions result from the perpendicular transport, enhanced in the case of $\sigma^2 = 1$, of EPs at the boundary between open and closed field lines that favors a net migration of EPs across the large-scale magnetic field from open to closed lines, due to the larger scattering mean free path in the weaker B-field of that region (see Equation (2)); after transferring onto a closed line, EPs precipitate in a nearly scatter-free regime along the closed lines toward the star surface. Due to the larger B-field (smaller mean free path at fixed σ^2) in the open lines region, the number of EPs migrating via perpendicular transport in the opposite direction, from closed to open, is smaller, as some can backscatter and return to a closed line. Along the open lines the EPs proceed in an outward trajectory toward the planet. The effect of a weaker turbulence ($\sigma^2 = 0.01$) is discussed below in this section.

As found in the case of TRAPPIST-1 (Fraschetti et al. 2019), for AU Mic the EP-depleted regions are explained by the combined effect of enhanced perpendicular diffusion and B-dependence of $\lambda_{||}$. The planet AU-Mic b is further out from the host star than TRAPPIST-1e, the closest HZ planet therein, i.e., 0.066 au compared with 0.029 au, but closer in units of stellar radius, 19 $R_\star$ compared with 52 $R_\star$; however, such differences do not lead to significant differences in the 2D histogram.

Figure 4 shows that, if EPs are injected further in ($R_s = 2\,R_\star$), the larger fraction of closed-to-open magnetic field lines in the inner wind increases the likelihood for EPs to be captured by the closed lines, and hence a smaller EP flux at the planet. The upper panels show the decrease with radius of EPs due to trapping by closed lines.

The combination of open field lines and strong turbulence focusses EPs into caps far out, allowing them to reach the planetary ecliptic. These caps track the high B-field projected region (see Figure 3). The high B-field shrinks the particle gyroscale, keeping them confined within a limited angle defining the caps. The magnetic field–rotation axis inclination angle of 19° (Klein et al. 2021b) causes the caps to be tilted toward the equatorial plane. Likewise, a magnetic field–rotation axis inclination angle of ∼40° in TRAPPIST-1 focusses EP caps toward the equatorial plane (Fraschetti et al. 2019). In case of alignment of the B-field and rotation axes, the projection of the CS would appear closer to the horizontal stripe in Figure 3 and the EP caps would be expected to be closer to the polar region.

The caps cross the equatorial plane, i.e., planetary orbits (Plavchan et al. 2020), implying a modulation in the bombardment of the planet and in the consequent atmospheric ionization rate. Likewise, a modulation of the EP flux at the HZ planet TRAPPIST-1e was found to be up to ∼4–5 orders of magnitude greater than experienced by Earth (Fraschetti et al. 2019), and its implications for the EP penetration depth were outlined by Fraschetti et al. (2021).

Also of interest is the timescale of particle modulation due to orbital motion and stellar rotation. The rotation period of AU Mic is shorter than the orbital period of the planets (8.46 days for AU Mic b; Klein et al. 2021b). The stellar rotation relative to the orbital motion will then sweep the EP caps over the planet with an effective period of approximately 11 days. The change in EP flux from the EP-depleted to EP-enhanced regions occurs over an azimuthal angle range of a few tens of degrees, such that the EP flux variation timescale would be of the order of a day. This is relevant for the recovery timescale of a planetary atmosphere to EP ionization events, and whether or not the atmosphere would be in a perturbed equilibrium state or subject to strong secular variation (Herbst et al. 2019; Chen et al. 2021).

The azimuthal variation of the EP flux impinging on the planet along its orbit around the star also strongly depends on the strength of the magnetic turbulence, as can be seen by comparing the case of strong (Figure 2) and weak turbulence (Figure 5). In the former case, the planet crosses two discernible caps, whereas in the latter the planet orbits into an azimuthally homogeneous, but much more sparse, distribution of EPs with far lower EP flux, evident also from the uniform color distribution in the latter. In the weak turbulence case, the distribution is closer to homogeneity as a result of the homogeneous injection on the R_s sphere and the boundary between closed and open field lines does not act as an attractor for EPs toward the stellar surface as in the case $\sigma^2 = 1$; a comparably homogeneous distribution was found in the case of the TRAPPIST-1 system (Fraschetti et al. 2019). The difference between the distributions in Figures 5 and 2 emphasizes the role of diffusion in the direction perpendicular to the large-scale unperturbed field that is not accounted for in a purely Monte Carlo approach to scattering off the magnetic fluctuations.

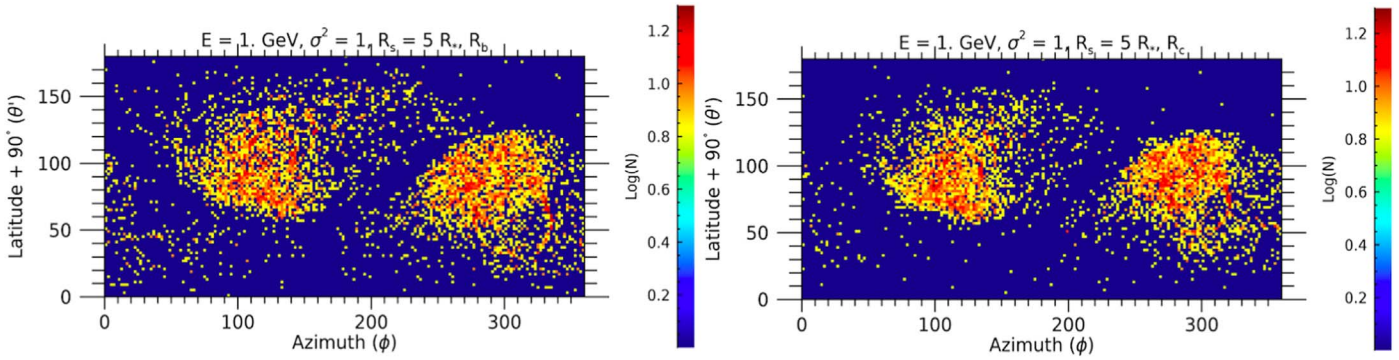

Figure 2. 2D histograms in spherical coordinates (in degrees) of the hitting points of 1 GeV kinetic energy protons injected at $R_s = 5\ R_\star$ into the quiescent stellar wind solution constructed from the ZDI radial field map from Klein et al. (2021b) for $\sigma^2 = 1$. The polar angle is defined as $\theta' = \theta + 90°$, where θ is the latitude centered on the star. The panels correspond to spherical surfaces at R_b (left) and R_c (right). Here, $L_c = 10^{-5}$ au. The planet's orbital plane corresponds here to a horizontal line at $\theta' = 90°$. The log-scale colorbar indicates the number of EPs within each $2° \times 2°$ pixel. The same total number of EPs was injected in each case shown below.

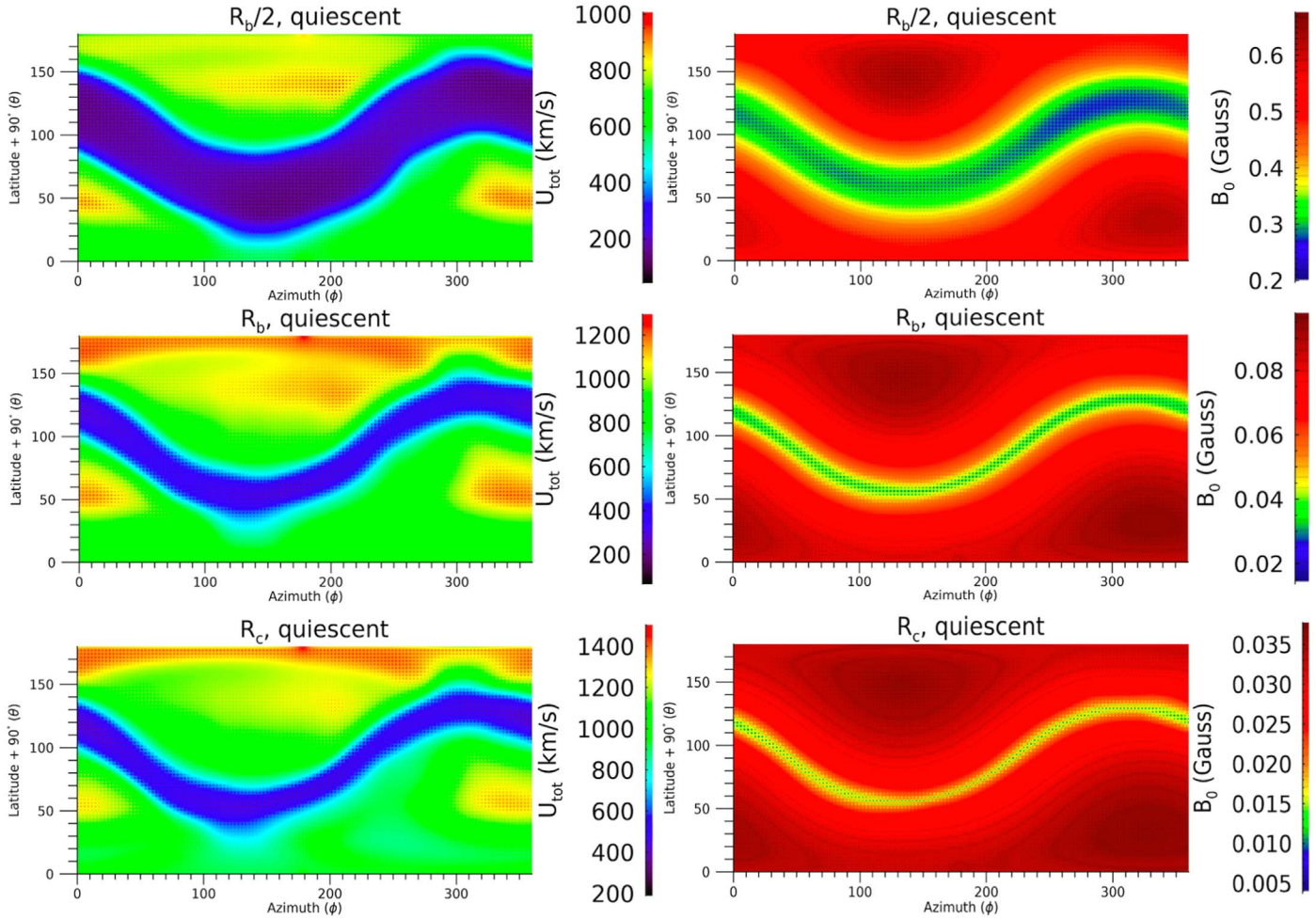

Figure 3. Top row: the total wind flow speed, U, (left) and magnitude of the unperturbed magnetic field, B_0, (right) in the quiescent wind solution driven by the ZDI map from Klein et al. (2021b) on the spherical surface at $R = R_b/2$. Middle row: same as the top row at $R = R_b$. Bottom row: same as the top row at $R = R_c$.

4.2. Energy-dependence of Particle Propagation

The spatial distribution of the EPs is fairly independent of the particle energy, as shown by comparing the 2D histograms for 0.1 GeV EPs (see Figure 6) with 1 GeV EPs (see Figure 2) at two distinct radii, for the same injection radius $R_s = 5\ R_\star$. As a consequence, an energy-dependence of the diffusion coefficient does not alter the EPs' 2D histograms. A comparison of the EP energy spectrum at various astrospheric distances requires spanning a wide range of EP energies, in order to include the effect of the perpendicular transport that solar in situ measurements suggest contribute significantly to circumsolar events (Fraschetti & Jokipii 2011; Gómez-Herrero et al. 2015). The present work focuses on the spatial distribution of EPs throughout the astrosphere and investigates the effect of the magnetic connection source-planet on the EP propagation. Transport might steepen the momentum spectrum

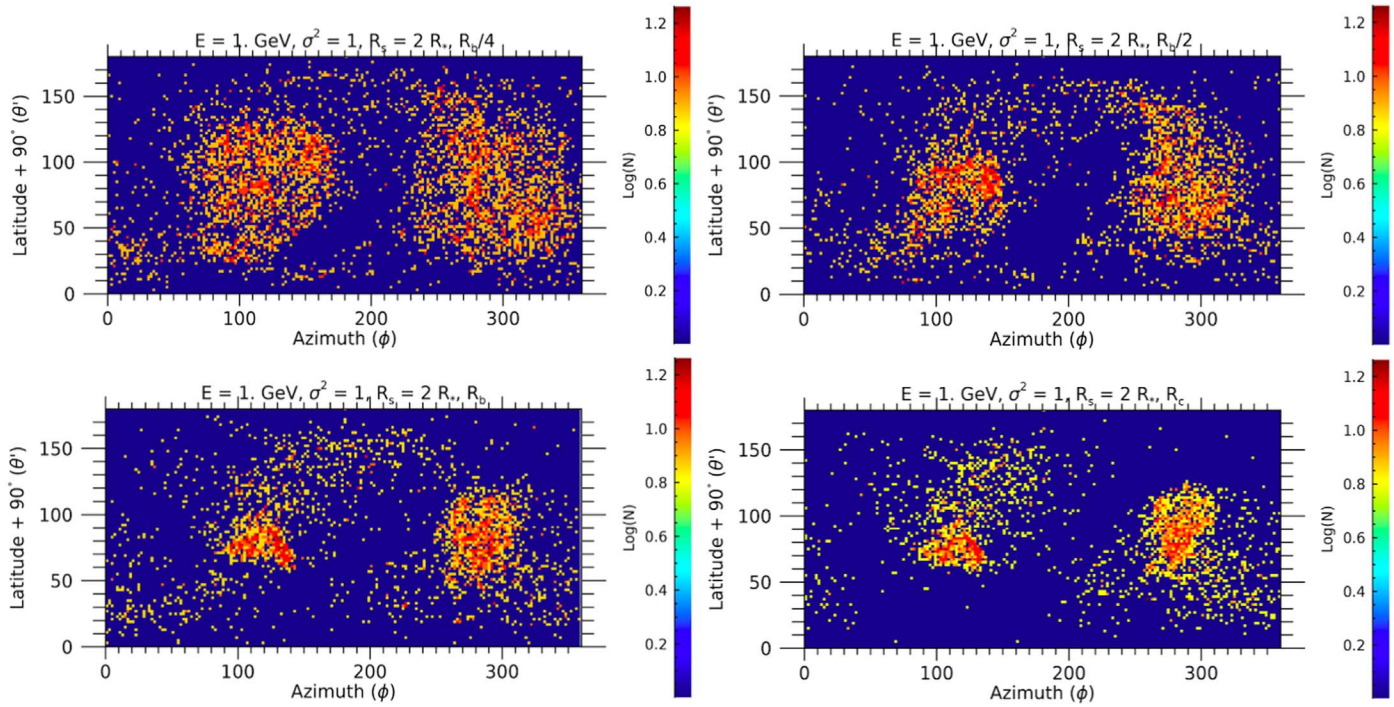

Figure 4. Same as Figure 2, except with particles injected closer in, at $R_s = 2\,R_\star = 1.04 \times 10^{11}$ cm $= 0.0069$ au. The panels corresponds to spherical surfaces at distinct radii: $0.25\,R_b = 4.8\,R_\star = 0.0165$ au (top left), $0.5\,R_b = 0.033$ au (top right), $R_b = 0.066$ au (bottom left), and $R_c = 0.11$ au (bottom right).

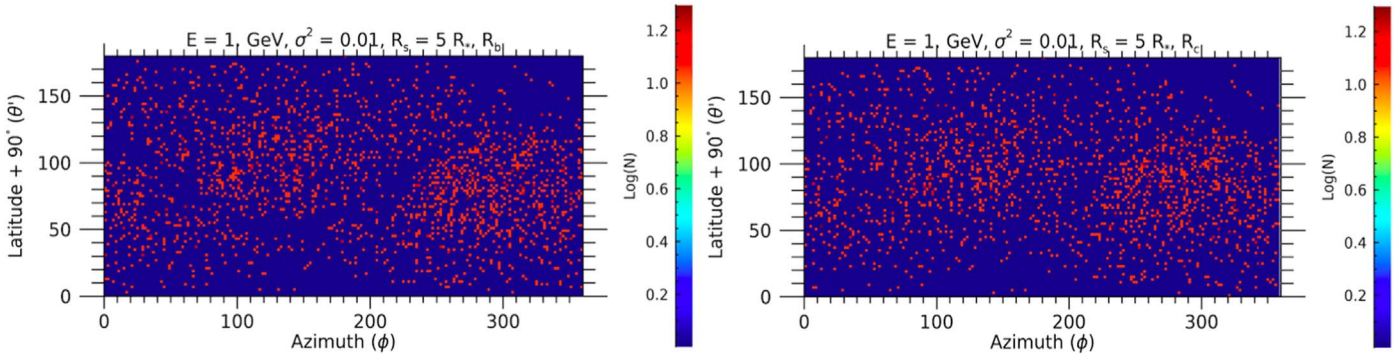

Figure 5. The same as Figure 2 except for a weaker turbulence of $\sigma^2 = 0.01$.

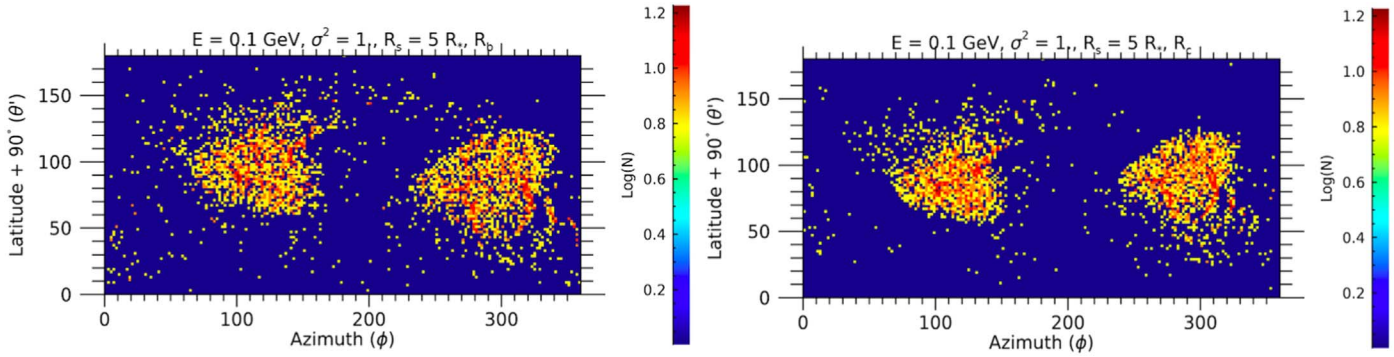

Figure 6. The same as Figure 2 except for $E = 0.1$ GeV.

of EPs at high energy, as shown with a pure scattering model with no perpendicular diffusion (Li & Lee 2015); however, spectral modifications are not investigated herein because the source of EPs is not localized to an individual shock with specified parameters, i.e., a fixed spectral shape.

4.3. EP Injection by Flares in the Stellar Corona

Although the structure of a flaring loop within a high-resistivity stellar corona cannot be produced by our ideal MHD simulations, we can mimick the flare-produced EPs by releasing them within $1R_\star$ from the stellar surface. Figure 7

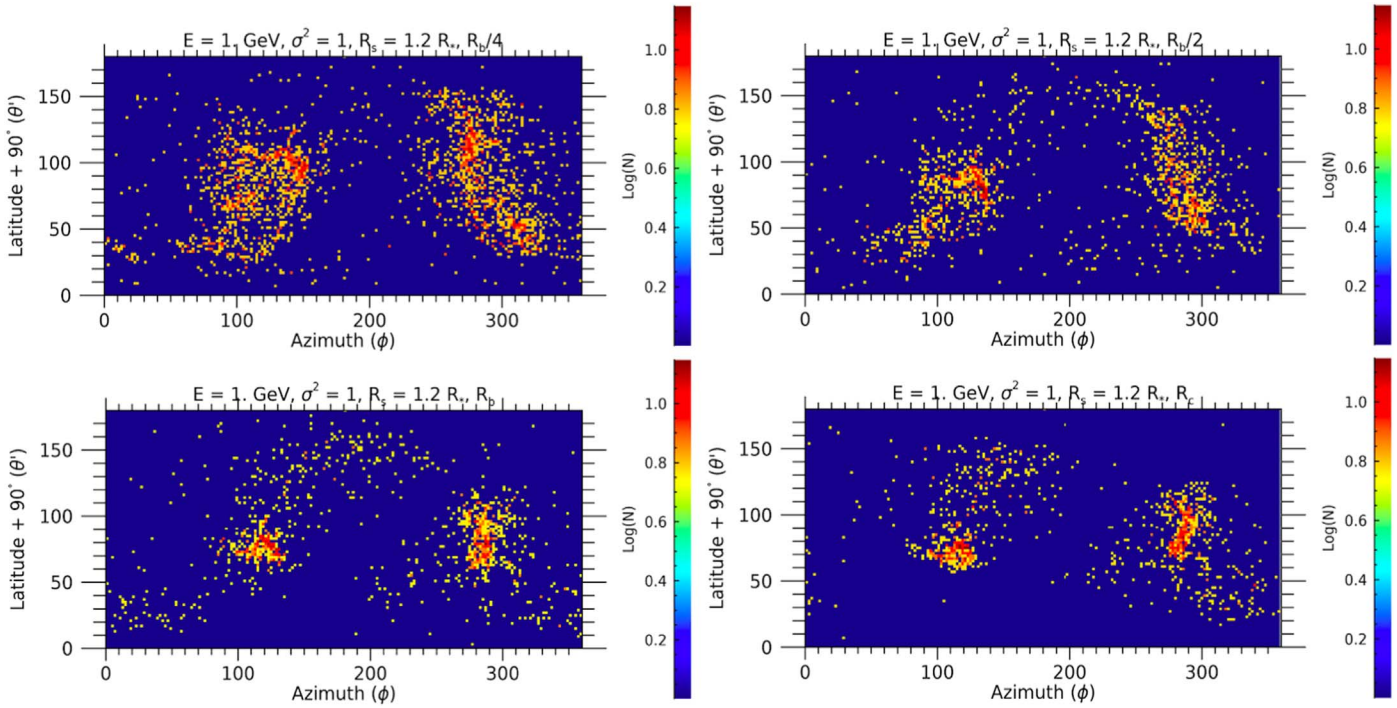

Figure 7. Same as Figure 2 but for $R_s = 1.2\,R_\star$ projected at $R = 0.25\,R_b$ (left top panel), $R = 0.5\,R_b$ (right top panel), at $R = R_b$ (left bottom panel), and at $R = R_c$ (right bottom panel).

depicts for the quiescent SW a 2D histogram at four distinct locations ($R = 0.25\,R_b$, $R = 0.5\,R_b$, R_b, and R_c) of EPs injected within the lower corona ($R_s = 1.2\,R_\star$), that represents flare-emitted EPs. The same EP pattern as at a larger injection radius of R_s is, including depleted regions, as wide as $\Delta\phi \sim 100°$. In the coronal region the magnetic field suppresses $\lambda_\parallel$ by about a factor of 10, favoring EP precipitation to the star from the open/closed lines boundary, as discussed above. The EP flux to the planet is as intense as for greater R_s, although is limited over two smaller azimuthal intervals, i.e., $\Delta\phi \sim 40°$ or $\sim$1 (or 2) days along the orbits of planet b (c).

4.4. Post-CME SW

In this section we present for the first time the propagation of EPs within the wind of a highly magnetized and active star 90 minutes after the eruption of a very energetic CME (see Figure 8). The CME is initiated by coupling AWSoM (van der Holst et al. 2014) and the Titov & Démoulin (1999) flux-rope eruption model, jointly used, for instance, to study fast CME-driven shocks with associated solar EP events (Jin et al. 2013). The initial conditions for the stellar wind are the same as considered for the quiescent state in Section 4.1 from Klein et al. (2021b). In addition, we have used as an initial condition the ZDI maps derived by Kochukhov & Reiners (2020), and show here only the result for the post-CME case. In particular, EPs are released on a spherical surface at radii of $R_s = 2$ and $5\,R_\star$, mimicking traveling shocks, at 90 minutes past the CME onset, as the CME front has crossed the entire simulation box.

EPs are assumed to diffuse into a turbulence with the same spectral index as the quiescent wind, as justified below. The CME is likely to stir up the parameters of the quiescent stellar wind turbulence more significantly the higher the CME kinetic energy becomes.

In the case of heliospheric CMEs, the power spectrum of the magnetic turbulence in the CME sheath (region between the shock front and the front of the CME driving it, crossed by a spacecraft typically in several hours) has been measured in situ at 1 au by the Wind spacecraft and analysed by Kilpua et al. (2021); a steepening of about 5%–10% of the inertial range power-law index for an interval of 2 hr was revealed, with a considerable data spread. However, the same statistical analysis has not been carried out for post-CME front turbulence, needed for a lag of a few hours in the present analysis.

In the case of EPs released at $R_s = 5\,R_\star \sim 2.5 \times 10^{11}$ cm the wind advection time to a certain radius R is $\Delta t(R) = (R - R_s)/\bar{U}$, where $\bar{U}$ is the average wind speed. Since the wind speed is highly variable in this region between $\sim$1000 and $\sim$5000 km s^{-1}, at the planet AU Mic b the time lapse along the stellar wind $\Delta t(R_b)$ is between 25 and 125 minutes and at the box boundary, $R_{\rm box} = 120\,R_\star = 6.0 \times 10^{12}$ cm, $\Delta t(R_{\rm box})$ is between 3 and 16 hr; thus, the parcel of wind plasma where EPs are released 90 minutes after the CME onset is likely to arrive at the box boundary between 3 and 16 hr after the CME front. As mentioned above, the heliospheric turbulence past the CME front has not been accurately investigated, so the turbulence seen by the EPs at the injection is not constrained by solar measurements. It is reasonable to assume that the pre-CME turbulence conditions (Kolmogorov isotropy) are restored in the parcel of gas, and at the time of EP release. An increase of the wind total magnetic field magnitude, with a wider spread, in heliospheric CMEs has also been measured by Kilpua et al. (2021); however, this effect is already accounted for in our 3D-MHD simulations.

Figure 9 (all panels in the left column) shows for weak turbulence ($\sigma^2 = 0.01$) a significantly different pattern from the nearly homogeneous distribution of the quiescent case: Figure 5 shows depleted regions partially corresponding with the CS silhouette and not significantly broadening between R_b

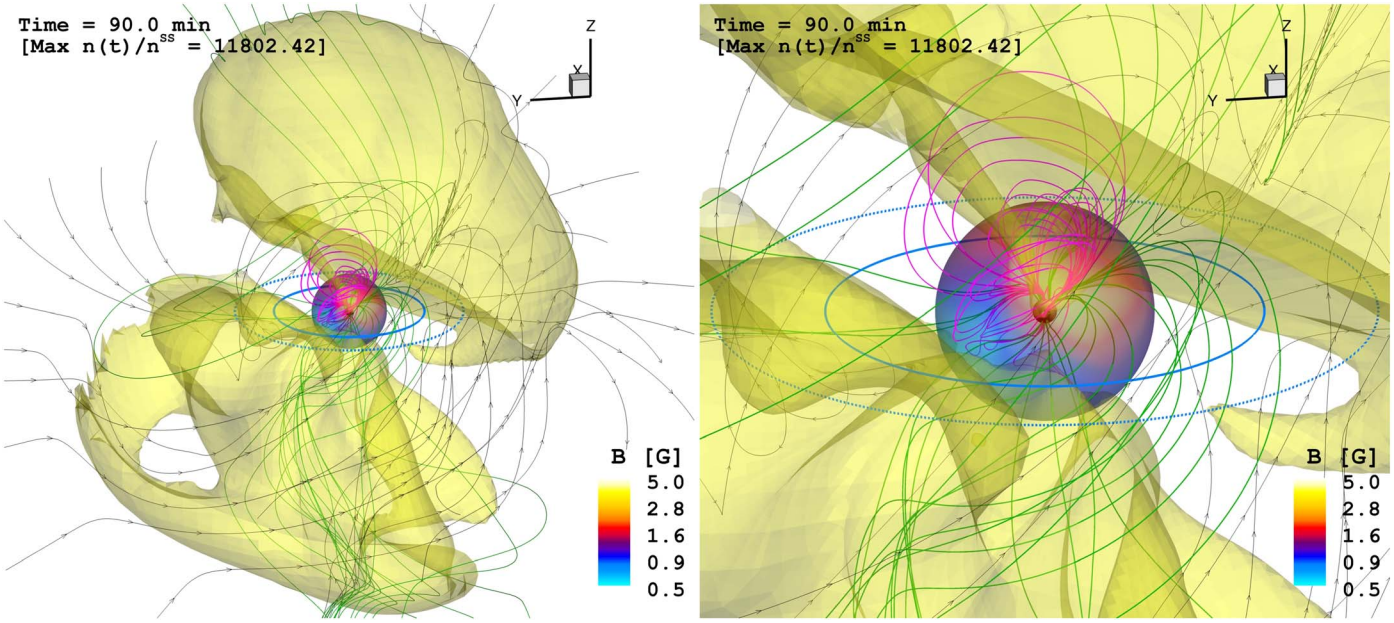

Figure 8. Left: snapshot in a 175 $R_\star$ field of view of the bi-lobed plasma density isosurface ($n(\mathbf{x}, t)/n_{SS}(\mathbf{x}) = 10.0$, where $n(\mathbf{x}, t)$ is the density at location $\mathbf{x}$ and time t and $n_{SS}(\mathbf{x})$ is the steady-state density at that location) of a propagating CME within wind reconstructed from the ZDI maps of Klein et al. (2021b) at a time 90 minutes past the CME initiation. The sphere at $R_b/2$ is color coded by the B-field strength. The two cyan circles represent the orbits of planet b (solid) and c (dotted). The magenta lines indicate selected closed magnetic field lines. Open magnetic field lines are in green if one end is attached to the star surface and in black if none of the ends is tracked, respectively. Right: same as the left panel with a 60 $R_\star$ field of view.

and R_c. As in the quiescent case of TRAPPIST-1 (Fraschetti et al. 2019), the near-homogeneity of the 2D histogram at $R = R_b$ (for $\sigma^2 = 0.01$) reflects the homogeneity of the injection of EPs on the injection sphere at R_s. In the post-CME case, the EPs distribution in the southern hemisphere mirrors the region of minimal B-strength (blue in Figure 10) only in a narrow depleted and tilted segment ($110° < \phi < 210°$; $50° < \theta < 70°$) in the mid- and bottom panels of Figure 9, in contrast with the quiescent case where the CME disrupts the large-scale structure of the B-field by distorting and pushing the CS away from its original location (compare the CS in Figure 1 with Figure 11, top and middle) and compressing the field strength by a factor up to a few tens from its quiescent value. Comparison of Figure 10 and Figure 3 shows such a CME-driven compression by a factor >10 throughout the astrosphere. The magnetic compression reduces throughout the astrosphere the EPs $\lambda_\parallel$ (by a factor $\sim 100^{1/3} \sim 4.6$; see Equation (2)).

Upon comparison of the right column, middle panel, of Figure 9 for the post-CME case (at $R = R_b$) with the case of the quiescent wind in Figure 2, EPs are channeled in the latter case into two polar caps connected by an axis tilted by $\sim$10–20° from the ecliptic plane. The asymmetry of the caps in the post-CME case, both largely in the southern hemisphere, results from the change in the large-scale B-field caused by the CME eruption. Figure 11 maps the 3D spatial location of the EPs hitting (spherical) points at the R_b sphere. Comparison of the EP locations with the B-field strength in the two top panels shows that the region with a relatively large and CME-compressed magnetic field on the sphere is EP-depleted (cfr., also with the EP-depleted regions in Figure 9) and corresponds to the launched high-density CME lobes (bottom panel in Figure 11). On the back side of the lobes the EPs fill the region with a lower magnetic field. We conclude that the rising CME inflates closed field lines in the direction of its motion (the CME cannot break field lines in our non-resistive MHD simulations) so that closed lines extend out to larger radii and expand sideway; as seen in the previous section, those closed lines cause the back precipitation of EPs to the star surface. On the back side (no CME lobes, no magnetic field compression) the EPs follow the open lines and escape toward the planets. Figure 9 shows also that the maximum EP flux is greater in the post-CME scenario than in the quiescent wind (see Figure 2).

5. Discussion

In Figure 12 the scattering mean free paths in units of the stellar radius ($\lambda_\parallel/R_\star$) as a function of $R/R_\star$ are compared for the innermost planets in AU Mic and for the innermost HZ TRAPPIST-1 planet. The smaller (by a factor $\sim$7) star radius but the greater (by a factor $\sim$3) surface average magnetic field (hence the smaller $\lambda_\parallel$ by a factor $\sim 3^{1/3}$) for TRAPPIST-1 so that at $R = R_s$ the mean free paths $\lambda_\parallel/R_\star$ have comparable values ($\sim$0.02), thereby explaining the comparable angular size of the depleted regions, i.e., vanishing EP flux, in the two systems.

The choice of a 90 minute post-CME snapshot does not require severe constraints on the flaring rate or more generally on the time lag between two transient events, i.e., very energetic CMEs or coronal flares. Consistently with the 90 minutes chosen, the TESS data indicate for AU Mic a flaring rate of $\sim$1 flare every 3.8 hr (Gilbert et al. 2022) for a flux at AU Mic b of 1.8×10^4 erg cm^{-2} s^{-1} sr^{-1} sr and 4.4×10^5 erg cm^{-2} s^{-1} sr^{-1} sr, respectively; this range reaches 30% the solar flux on Earth (i.e., 1, 373 W m^{-2}).

A comparison of the spatial distribution of the EPs at distances of $R_b/2$, R_b, and R_c for $\sigma^2 = 0.01$ in the quiescent and in the post-CME case (Figures 9 and 5), shows that, if a CME escapes, the closed magnetic field lines are inflated and hence efficiently trap EPs (in the region $\theta' > 50°$, $\phi < 100°$, and $\phi \gtrsim 280°$); moreover, the reshuffling of the large-scale

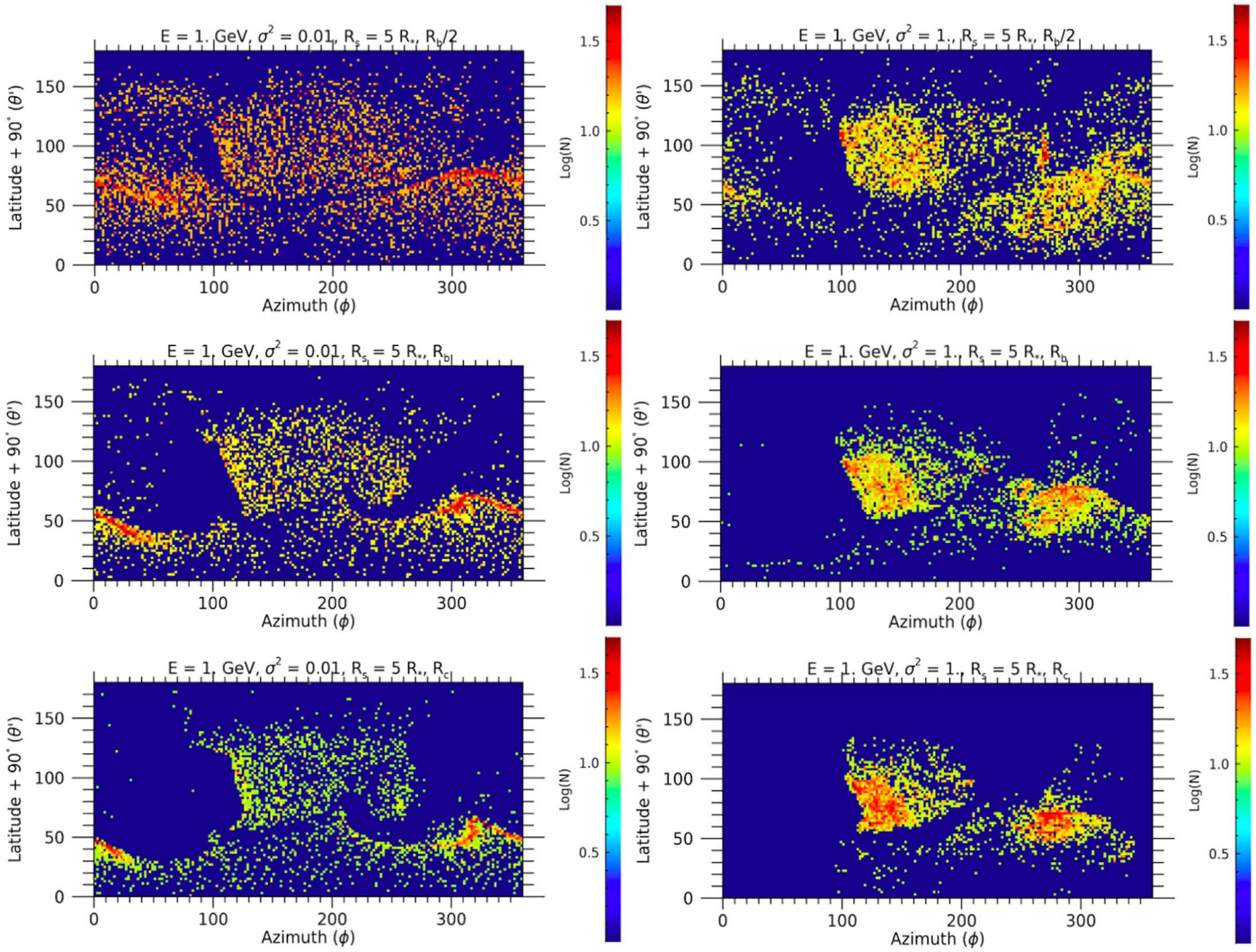

Figure 9. Top row: for a stellar wind 90 minutes past the eruption of a 10^{36} erg kinetic energy CME, spherical-coordinates 2D EP histogram at radii of $R = R_b/2$ (top row), $R = R_b$ (mid row), and $R = R_c$ (bottom row) of the hitting points for 1 GeV kinetic energy protons, for $\sigma^2 = 0.01$ (left column) and $\sigma^2 = 1$ (right column), injected at $R_s = 5\,R_\star$; here $L_c = 10^{-5}$ au. The quiescent stellar wind is constructed from the ZDI radial field map from Klein et al. (2021b). The x (y) axis indicates the azimuthal (polar) coordinate on that sphere. The log-scale colorbar counts logarithmically the number of EPs. Bottom row: same as the top row but for $R = R_b$.

magnetic field caused by the CME opens regions of the southern hemisphere to EPs, deflecting them toward hot spots (in red at $30° < \theta' < 60°$, $0° < \phi < 40°$ and $50° < \theta' < 70°$, $\phi > 280°$) from the equatorial plane. This trapping effect by the expanding CME is shown for the strong turbulence case in Figure 11. The angular location of the EP hot spots (red regions in Figure 9) depends on the spatial initialization of the CME, whose choice herein refers to AU Mic observations (Wisniewski et al. 2019); a different CME initialization might drive a more intense or weaker EP flux toward the planets. This result might seem in contrast with the expectation that the CMEs open and stretch out magnetic field lines providing additional routes for EPs to reach the planets; however, a resistive non-ideal MHD simulation would be necessary to overcome such a limitation. We have carried out multiple runs with distinct single realizations of the magnetic turbulence with no significant deviation from the conclusion above.

Figure 13 (left panel), shows that the EP number at radius R relative to $N_{\rm inj}$ at each distance is enhanced by the prior passage of a CME for $\sigma^2 = 0.01$, and lowered for $\sigma^2 = 1$, for the magnetic field reconstruction in Klein et al. (2021a)'s map. This inversion can be explained as follows. The CME inflates the closed field lines out to a large distance from the star and reshuffles the closed field lines (see Figure 11, top row) in a pattern dependent on the location of the CME initialization region with respect to the CS. If $\sigma^2 = 0.01$, the EPs follow the field lines with little scattering (see Figure 12), reach larger distances along the closed lines, i.e., travel a longer time, and are therefore more likely to migrate to open lines and escape to the planets; thus, the EP flux is greater than the quiescent case. In the case $\sigma^2 = 1$, the number of EPs arriving at the planets does not increase with respect to the case $\sigma^2 = 0.01$ as much as in the quiescent case; the migration from closed to open field lines due to the perpendicular diffusion is suppressed as the post-CME chaotic structure of the field lines dominates over the transport (see Section 4.1).

Figure 13 (right panel) shows the relative EP number obtained with an identical spatial CME initialization to the left panel and the magnetic field map of Kochukhov & Reiners (2020). In addition, a different turbulence realization (with the same statistical properties) from the left panel was used

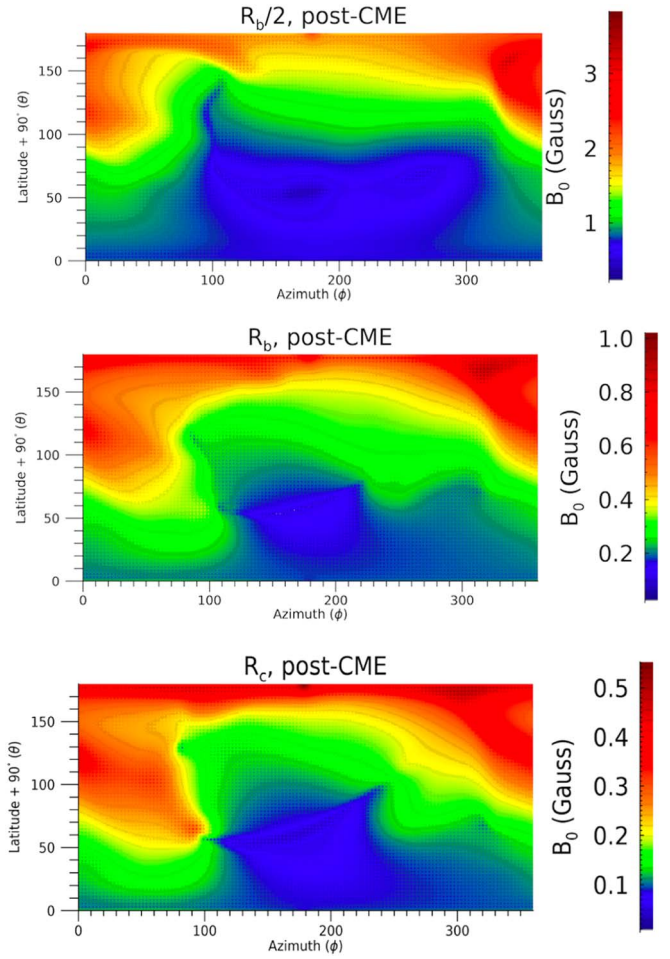

Figure 10. Top: in the 90 minutes post-CME snapshot based on the Klein et al. (2021b) magnetogram as in Figure 8, the strength of the unperturbed wind magnetic field B_0 projected on the spherical surface at $R = R_b/2$, with azimuthal (polar) coordinates degrees on that sphere, is indicated on the x (y) axis. Middle: same as the top left but at a radius of $R = R_b$. Bottom: same as the top left but at a radius of $R = R_c$.

(Fraschetti & Giacalone 2012) to show that the $N(R)/N_{\rm inj}$ increase with σ^2 is not dependent on the particular details of the turbulence (simulations using the turbulence ensemble average are not shown as the EP distribution is nearly homogeneous with a smaller EP flux onto the planets, and is thus not relevant to the present study). For the Kochukhov & Reiners (2020) map, the slope of the EP number versus σ^2 is comparable to the slope for the Klein et al. (2021a) field because the chaotic large-scale structure of the post-CME field dominates over transport. This comparison shows that different conditions can lead to very different EP numbers at a given radius, and likely to a different planet bombardment, after the passage of the CME.

As pointed out above, the perhaps unlikely CME escape from such a magnetically confining star, as well as the technical limitations in confirming CMEs from active stars, led to extrapolations of the coronal flare/CME relation from the solar system to M dwarfs. However, the tension between the low mass-loss rate associated with M dwarfs (Wood et al. 2021) and the wind flux required to support a very energetic CME (Drake et al. 2013) seems to indicate that flares should be more

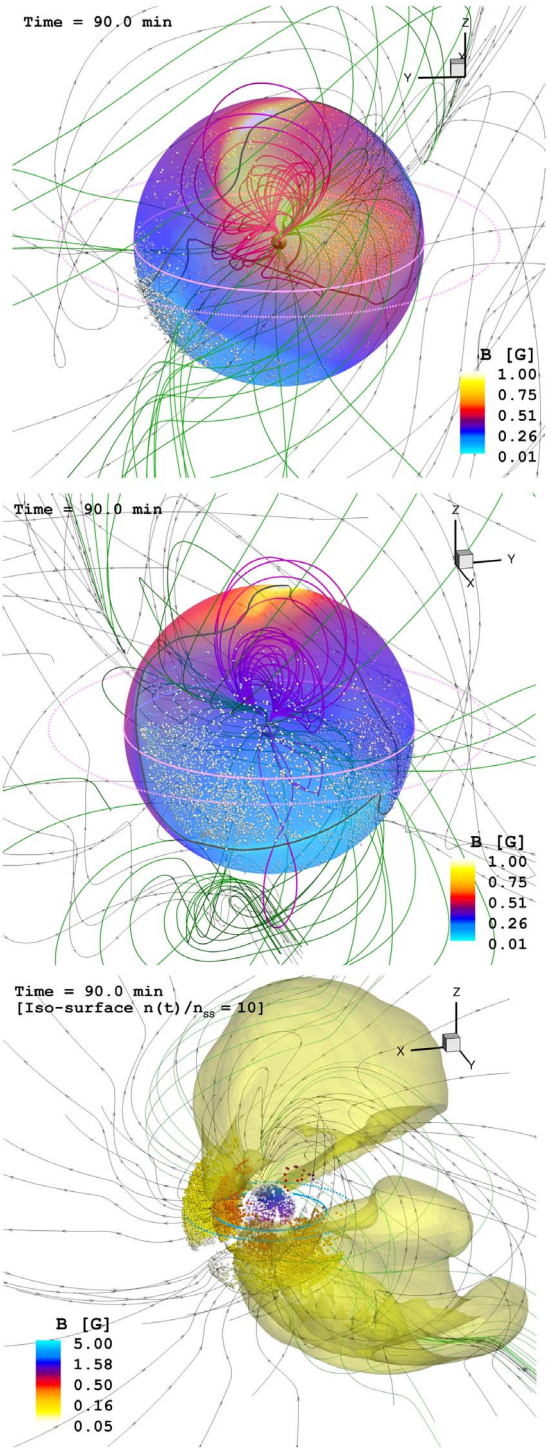

Figure 11. Top: in the 90 minutes post-CME case based on the Klein et al. (2021b) magnetogram as in Figure 8, the EP hitting points on the R_b sphere are seen from the side of the two CME expanding lobes. The strength of the unperturbed wind magnetic field B_0 color codes the R_b sphere. The two magenta circles represent the orbits of planet b (solid) and c (dotted). The purple lines indicate selected closed magnetic field lines. Open magnetic field lines are in green or black if one end is attached to the star surface or if none of the ends is tracked, respectively. Middle: same as the top left but from the back side. Bottom: snapshot in a 180 $R_\star$ field of view of the bi-lobed plasma density isosurface $(n(\mathbf{x},\ t)/n_{SS}(\mathbf{x}) = 10.0)$ of the propagating CME within the wind reconstructed from the ZDI maps of Klein et al. (2021b) at 90 minutes past the CME initiation. The spherical dots at $R_b/2$, R_b, and R_c mark the EP hitting points and are color coded by the B-field strength. The two cyan circles represent the orbits of planet b (solid) and c (dotted). Open magnetic field lines are in black.

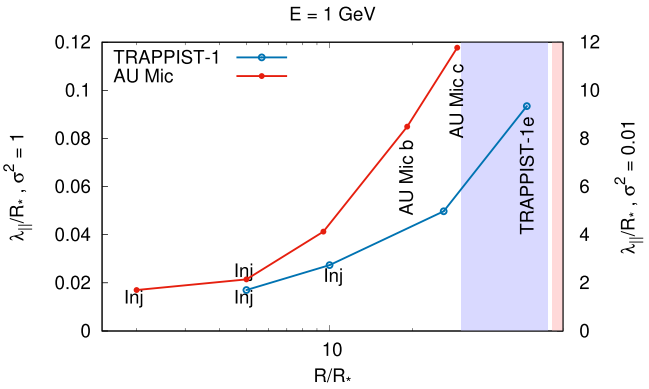

Figure 12. Comparison of the 1 GeV proton scattering mean free path as a function of radial distance from the host star, both in units of $R_\star$, for quiescent AU Mic (magnetogram from Klein et al. 2021b) and TRAPPIST-1 (Fraschetti et al. 2019), for $\sigma^2 = 1$ (left y-axis) and for $\sigma^2 = 0.01$ (right y-axis) at four locations for TRAPPIST-1 and five for AU Mic. Two values of R_s ("Inj") are seen, the half and full radius of AU Mic b's orbit and semimajor axis of TRAPPIST-1e and AU Mic c. The value of $\lambda_\parallel$ is calculated from Equation (2) by using a typical magnetic field strength at the boundary between the CS stripe and the open field lines region, as inferred from the maps in Figure 3 and in Figure 10 of Fraschetti et al. (2019). The red/blue (AU Mic/TRAPPIST-1) shaded areas indicate the HZs from the inner boundary (0.22 au for AU Mic and 0.017 au for TRAPPIST-1) to the outer boundary (0.035 au for TRAPPIST-1).

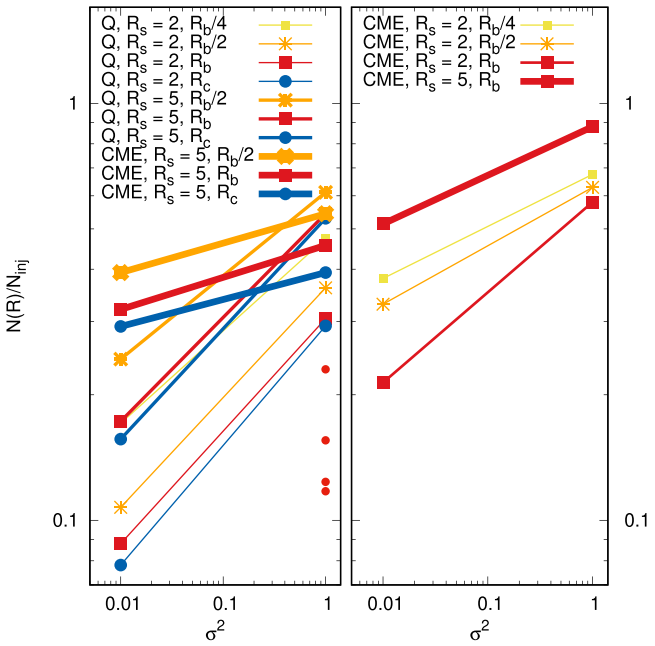

Figure 13. Left: fraction of 1 GeV EPs reaching a given sphere at radius R to the total number of injected EPs, $N_{\rm inj}$ as a function of σ^2 in the stellar wind reconstructed from the ZDI maps of Klein et al. (2021b). The quiescent case (labeled as "Q") is compared with the 90 minutes post-CME case ("CME"). The red filled circles refer to the flare case ($R_s = 1.2\,R_\star$; Figure 7) corresponding, from lowest to highest $N(R)/N_{\rm inj}$ to $R = 0.15R_b$, $R_b/4$, $R_b/2$, and R_b. Right: same as the left panel but for the stellar wind reconstructed from the ZDI maps of Kochukhov & Reiners (2020), case 1 from (Alvarado-Gómez et al. 2022), in the 90 minutes post-CME case.

common than CMEs; hence, a large fraction of EPs impinging onto planets might be released very close to the stellar surface by coronal flares rather than from CMEs. The lack of radio bursts resembling solar type II bursts (Villadsen & Hallinan 2019) supports such a conclusion. In addition, in CME simulations shocks are generated further out in the corona, where densities are considerably smaller than in the solar region of type II burst formation and frequencies below the detection threshold (Alvarado-Gómez et al. 2020). This effect is partially compensated by the relatively small flux of EPs emitted in the lower corona and reaching the planets (Figure 13, left panel, red filled circles for $\sigma^2 = 1$).

The time-variability of the flux of stellar EPs and its effect on the planetary atmosphere (Fraschetti et al. 2019; Herbst et al. 2019), as well as on the ionization of proto-planetary disks around young stars (Rodgers-Lee et al. 2017; Fraschetti et al. 2018; Padovani et al. 2018), has been under increasing scrutiny in the past few years. The evolution of planetary atmospheres can be also affected by Galactic cosmic rays (GCRs), that are likely unmodulated by the stellar wind at energies >1–10 GeV. Several works have considered the effect of stellar wind on the energy spectrum of GCRs impinging onto the planet, e.g., Archean Earth (Cohen et al. 2012) or exoplanets (Herbst et al. 2020; Mesquita et al. 2022). The ∼0.3 GeV EP propagation and modulation has been long known to be dominated by drifts in the solar system (Jokipii et al. 1977); any calculation of stellar modulation in such an energy range needs to account for drifts (Mesquita et al. 2022). However, for the solar system the flux of protons at 0.1–0.7 GeV during ground level enhancement (GLE) events exceeds typically by 1 or 2 orders of magnitude the GCR flux, at 1 au. For active stars, likely producing many more energetic events than the Sun, the flux of stellar EPs at distances <1 au (planets b and c in AU Mic and HZ planets in TRAPPIST-1) is likely to be much higher than the local GCR flux, even including the adiabatic losses due to the radially expanding wind (Youngblood et al. 2017). The higher energy range of GCRs (>1–10 GeV) than stellar EPs might partially compensate the much lower flux of GCRs in the effect on the atmosphere evolution of the inner planets. Such impact on the global planet atmosphere (Segura et al. 2010; Airapetian et al. 2016) has to be investigated in further detail.

Figure 14 shows that the EP flux along the planetary orbit undergoes orders of magnitude fluctuations, as was also shown in the TRAPPIST-1 case (Fraschetti et al. 2019). Likewise, we calculate here the flux of EPs impinging onto the planet by using the estimate of a >10 MeV proton flux inferred for GJ 876 by Youngblood et al. (2017). The flux in the ecliptic plane is determined within a ring of semi-latitude aperture of 5° (despite the near-complanarity of the planet), to determine the flux of EPs in the planetary environment. The cases of quiescent wind and 90 minutes post CME are compared in Figure 14 for 1 GeV protons at the AU Mic b orbit. In the case of the post CME, only ∼5% (∼1%) of the total injected EPs hit the ring enclosing the planet orbit for strong (weak) turbulence as the large part of the EPs travel toward other latitudes. The low EP flux in the plane of the planetary orbits results from the particular geometry of the fluxtube setup. This is due to initialization of the CME at low latitudes, suggested by observations (Wisniewski et al. 2019), perhaps contrary to expectation. The expansion of the CME inflates closed field lines over a vast angular region that includes the equatorial plane, preventing the escape of EPs toward the planets. It is conceivable that with a smaller misalignment between the B-field and stellar rotation axis, CME lobes travel poleward and the EPs emitted subsequently

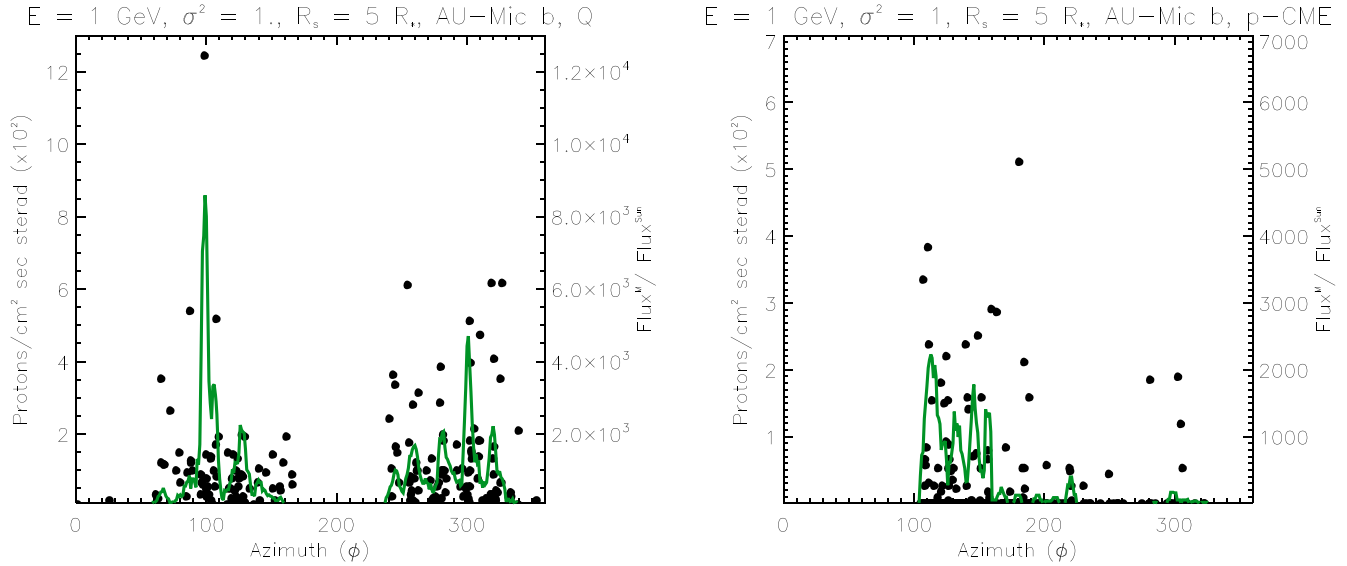

Figure 14. Left: flux of 1 GeV protons (magnetogram from Klein et al. 2021b) impinging onto a latitudinal ring of semiaperture $\Delta\theta = 5°$ centered on the equatorial plane at radius $R = R_b$ in a quiescent wind for the strong turbulence case of $\sigma^2 = 1$. An azimuthal binning of 1° is used and the green overlayed curve is a smoothed average with a 5° smoothing width. The left-hand side *y*-axis provides the EP flux rescaled to the peak of the HZ planet of GJ 876 (see Section 5). The right-hand side *y*-axis uses a crudely approximated renormalization to the solar EP flux based on a flaring rate estimate. Right: same as the left panel but for the case of a 90 minutes post-CME eruption.

might more easily be magnetically connected to the planets along open field lines.

6. Conclusion

We have carried out numerical simulations of the propagation of ∼GeV protons out to the two innermost planets in the reconstructed astrosphere of the dM1e star AU Microscopii, for the first time both in the quiescent and CME-disrupted state. Energetic particles are injected at a variety of distances from the star on spherical surfaces with an isotropic velocity distribution and diffuse in the turbulent stellar magnetic field.

The post-CME wind is likely to be the most common stellar wind configuration of very active stars encountered by propagating EPs due to the very high flaring rate; however, large stellar magnetic fields hamper CME escape and observational constraints on the rate of escaped CME are currently lacking. We determine the spherical pattern of EPs reaching the distances of planets b and c; the projection of the CS at the planetary distance maps the back precipitation of EPs to the star and is enhanced by perpendicular diffusion in the strong turbulence regime.

The CME eruption reshuffles the dipolar structure of the large-scale magnetic field and dominates over the magnetic turbulence in controlling the EP flux at least 90 minutes after its eruption; as a result, the bombardment of planets by the EPs released after the CME passage can be suppressed or enhanced by the CME. A stronger turbulence leads instead in all cases to a larger EP flux at the planets. We emphasize that, even for very energetic and wide-front CMEs such as the one examined here, the EP flux along the planetary orbits depends on the region of the CME initialization, similar to the case of solar CMEs.

The effect of EPs released by CME-driven shocks localized to small spatial regions has not been considered here but deserves merits future investigation.

We thank the referee for useful and constructive comments. F.F. was supported, in part, by NASA through Chandra Theory Award Number *TM*0 − 21001*X*, *TM*6 − 17001*A* issued by the Chandra X-ray Observatory Center, which is operated by the Smithsonian Astrophysical Observatory for and on behalf of NASA under contract NAS8-03060; F.F. is also partially supported by NASA under Grants NNX16AC11G and 80NSSC18K1213 and by NSF under grant 1850774. J.J.D. was supported by NASA contract NAS8-03060 to the Chandra X-ray Center and thanks the Director, Pat Slane, for continuing advice and support. O.C. is supported by NASA XRP grant 80NSSC20K0840. Resources supporting this work were provided by the NASA High-End Computing (HEC) Program through the NASA Advanced Supercomputing (NAS) Division at Ames Research Center.

ORCID iDs

Federico Fraschetti https://orcid.org/0000-0002-5456-4771
Julián D. Alvarado-Gómez https://orcid.org/0000-0001-5052-3473
Jeremy J. Drake https://orcid.org/0000-0002-0210-2276
Ofer Cohen https://orcid.org/0000-0003-3721-0215
Cecilia Garraffo https://orcid.org/0000-0002-8791-6286

References

Addison, B. C., Horner, J., Wittenmyer, R. A., et al. 2021, AJ, 162, 137
Airapetian, V. S., Glocer, A., Gronoff, G., Hébrard, E., & Danchi, W. 2016, NatGe, 9, 452
Alvarado-Gómez, J. D., Cohen, O., Drake, J. J., et al. 2022, ApJ, 928, 147
Alvarado-Gómez, J. D., Drake, J. J., Cohen, O., Moschou, S. P., & Garraffo, C. 2018, ApJ, 862, 93
Alvarado-Gómez, J. D., Drake, J. J., Fraschetti, F., et al. 2020, ApJ, 895, 47
Alvarado-Gómez, J. D., Drake, J. J., Moschou, S. P., et al. 2019, ApJL, 884, L13
Argiroffi, C., Reale, F., Drake, J. J., et al. 2019, NatAs, 3, 742
Armstrong, J. W., Rickett, B. J., & Spangler, S. R. 1995, ApJ, 443, 209
Belov, A., Kurt, V., Mavromichalaki, H., & Gerontidou, M. 2007, SoPh, 246, 457
Burlaga, L. F., & Turner, J. M. 1976, JGR, 81, 73

Chen, H., Zhan, Z., Youngblood, A., et al. 2021, NatAs, 5, 298
Cohen, O., Alvarado-Gomez, J. D., Drake, J. J., et al. 2022, ApJ, 934, 189
Cohen, O., Drake, J. J., & Kóta, J. 2012, ApJ, 760, 85
Cohen, O., Garraffo, C., Moschou, S. P., et al. 2020, ApJ, 897, 101
Cohen, O., Kashyap, V. L., Drake, J. J., et al. 2011, ApJ, 733, 67
Cohen, O., Sokolov, I. V., Roussev, I. I., et al. 2008, JASTP, 70, 583
Cully, S. L., Fisher, G. H., Abbott, M. J., & Siegmund, O. H. W. 1994, ApJ, 435, 449
David, L., Fraschetti, F., Giacalone, J., et al. 2022, ApJ, 928, 66
Drake, J. J., Cohen, O., Yashiro, S., & Gopalswamy, N. 2013, ApJ, 764, 170
Dröge, W., Kartavykh, Y. Y., Dresing, N., & Klassen, A. 2016, ApJ, 826, 134
Dröge, W., Kartavykh, Y. Y., Klecker, B., & Kovaltsov, G. A. 2010, ApJ, 709, 912
Evensberget, D., Carter, B. D., Marsden, S. C., Brookshaw, L., & Folsom, C. P. 2021, MNRAS, 506, 2309
Fitz Axen, M., Offner, S. S. S., Gaches, B. A. L., et al. 2021, ApJ, 915, 43
Fraschetti, F. 2016a, PhRvE, 93, 013206
Fraschetti, F. 2016b, ASTRP, 2, 63
Fraschetti, F., Drake, J., Gronoff, G., et al. 2021, BAAS, 53, 1210
Fraschetti, F., Drake, J. J., Alvarado-Gómez, J. D., et al. 2019, ApJ, 874, 21
Fraschetti, F., Drake, J. J., Cohen, O., & Garraffo, C. 2018, ApJ, 853, 112
Fraschetti, F., & Giacalone, J. 2012, ApJ, 755, 114
Fraschetti, F., & Jokipii, J. R. 2011, ApJ, 734, 83
Fulton, B. J., Petigura, E. A., Howard, A. W., et al. 2017, AJ, 154, 109
Gaches, B. A. L., & Offner, S. S. R. 2018, ApJ, 861, 87
Gaia Collaboration, Brown, A. G. A., Vallenari, A., et al. 2018, A&A, 616, A1
Garraffo, C., Drake, J. J., Cohen, O., Alvarado-Gómez, J. D., & Moschou, S. P. 2017, ApJL, 843, L33
Giacalone, J., & Jokipii, J. R. 1999, ApJ, 520, 204
Gilbert, E. A., Barclay, T., Quintana, E. V., et al. 2022, AJ, 163, 147
Goldreich, P., & Sridhar, S. 1995, ApJ, 438, 763
Gombosi, T. I., van der Holst, B., Manchester, W. B., & Sokolov, I. V. 2018, LRSP, 15, 4
Gómez-Herrero, R., Dresing, N., Klassen, A., et al. 2015, ApJ, 799, 55
Herbst, K., Grenfell, J. L., Sinnhuber, M., et al. 2019, A&A, 631, A101
Herbst, K., Papaioannou, A., Airapetian, V. S., & Atri, D. 2021, ApJ, 907, 89
Herbst, K., Scherer, K., Ferreira, S. E. S., et al. 2020, ApJL, 897, L27
Horbury, T. S., & Tsurutani, B. 2001, in Ulysses Measurements of Waves, Turbulence and Discontinuities, ed. A. Balogh, R. G. Marsden, & E. J. N. Y. S.-V. Smith (Berlin: Springer), 167
Houdebine, E. R., Foing, B. H., & Rodono, M. 1990, A&A, 238, 249
Hu, J., Airapetian, V. S., Li, G., Zank, G., & Jin, M. 2022, SciA, 8, eabi9743
Hu, R., Damiano, M., Scheucher, M., et al. 2021, ApJL, 921, L8
Jackman, J. A. G., Wheatley, P. J., Acton, J. S., et al. 2020, MNRAS, 497, 809
Jin, M., Manchester, W. B., van der Holst, B., et al. 2013, ApJ, 773, 50
Jokipii, J. R. 1966, ApJ, 146, 480
Jokipii, J. R., & Coleman, P. J., Jr 1968, JGR, 73, 5495
Jokipii, J. R., Levy, E. H., & Hubbard, W. B. 1977, ApJ, 213, 861
Kalas, P., Liu, M. C., & Matthews, B. C. 2004, Sci, 303, 1990
Katsova, M. M., Drake, J. J., & Livshits, M. A. 1999, ApJ, 510, 986
Kavanagh, R. D., Vidotto, A. A., Klein, B., et al. 2021, MNRAS, 504, 1511
Kilpua, E. K. J., Good, S. W., Ala-Lahti, M., et al. 2021, FrASS, 7, 109
Klein, B., Donati, J.-F., Hébrard, E. M., et al. 2021a, MNRAS, 500, 1844
Klein, B., Donati, J.-F., Moutou, C., et al. 2021b, MNRAS, 502, 188
Kochukhov, O., & Reiners, A. 2020, ApJ, 902, 43
Li, G., & Lee, M. A. 2015, ApJ, 810, 82
Magee, H. R. M., Güdel, M., Audard, M., & Mewe, R. 2003, AdSpR, 32, 1149
Martioli, E., Hébrard, G., Correia, A. C. M., Laskar, J., & Lecavelier des Etangs, A. 2021, A&A, 649, A177
Mesquita, A. L., Rodgers-Lee, D., Vidotto, A. A., & Kavanagh, R. D. 2022, MNRAS, 515, 1218
Moschou, S.-P., Drake, J. J., Cohen, O., et al. 2019, ApJ, 877, 105
Ó Fionnagáin, D., Kavanagh, R. D., Vidotto, A. A., et al. 2022, ApJ, 924, 115
Owen, J. E., & Wu, Y. 2013, ApJ, 775, 105
Padovani, M., Ivlev, A. V., Galli, D., & Caselli, P. 2018, A&A, 614, A111
Paudel, R. R., Barclay, T., Schlieder, J. E., et al. 2021, ApJ, 922, 31
Pierrehumbert, R., & Gaidos, E. 2011, ApJL, 734, L13
Plavchan, P., Barclay, T., Gagné, J., et al. 2020, Natur, 582, 497
Plavchan, P., Werner, M. W., Chen, C. H., et al. 2009, ApJ, 698, 1068
Powell, K. G., Roe, P. L., Linde, T. J., Gombosi, T. I., & De Zeeuw, D. L. 1999, JCoPh, 154, 284
Rab, C., Güdel, M., Padovani, M., et al. 2017, A&A, 603, A96
Redfield, S., Linsky, J. L., Ake, T. B., et al. 2002, ApJ, 581, 626
Rodgers-Lee, D., Taylor, A. M., Ray, T. P., & Downes, T. P. 2017, MNRAS, 472, 26
Sachdeva, N., Tóth, G., Manchester, W. B., et al. 2021, ApJ, 923, 176
Sachdeva, N., van der Holst, B., Manchester, W. B., et al. 2019, ApJ, 887, 83
Segura, A., Walkowicz, L. M., Meadows, V., Kasting, J., & Hawley, S. 2010, AsBio, 10, 751
Telloni, D., Carbone, F., Bruno, R., et al. 2019, ApJ, 887, 160
Titov, V. S., & Démoulin, P. 1999, A&A, 351, 707
Torres, C. A. O., Ferraz Mello, S., & Quast, G. R. 1972, ApL, 11, 13
Tóth, G., Sokolov, I. V., Gombosi, T. I., et al. 2005, JGRA, 110, A12226
van der Holst, B., Huang, J., Sachdeva, N., et al. 2022, ApJ, 925, 146
van der Holst, B., Sokolov, I. V., Meng, X., et al. 2014, ApJ, 782, 81
Veronig, A. M., Odert, P., Leitzinger, M., et al. 2021, NatAs, 5, 697
Vida, K., Kővári, Z., Pál, A., Oláh, K., & Kriskovics, L. 2017, ApJ, 841, 124
Vida, K., Leitzinger, M., Kriskovics, L., et al. 2019, A&A, 623, A49
Vidotto, A. A., Fares, R., Jardine, M., Moutou, C., & Donati, J. F. 2015, MNRAS, 449, 4117
Villadsen, J., & Hallinan, G. 2019, ApJ, 871, 214
Wisniewski, J. P., Kowalski, A. F., Davenport, J. R. A., et al. 2019, ApJL, 883, L8
Wood, B. E., Mueller, H.-R., Redfield, S., et al. 2021, ApJ, 915, 37
Youngblood, A., France, K., Loyd, R. O. P., et al. 2017, ApJ, 843, 31
Zhao, L. L., Zank, G. P., Adhikari, L., et al. 2020, ApJ, 898, 113